Effect of the star formation histories on the SFR-M-* relation at z ≥ 2

L. P. Cassara, D. Maccagni, B. Garilli, M. Scodeggio, R. Thomas, O. Le Fevre, G. Zamorani, D. Schaerer, B. C. Lemaux, P. Cassata, et al.

Effect of the star formation histories on the *SFR-M*$_*$ relation at $z \geq 2$

L. P. Cassarà[1,19], D. Maccagni[1], B. Garilli[1], M. Scodeggio[1], R. Thomas[3], O. Le Fèvre[3], G. Zamorani[2], D. Schaerer[10,8], B. C. Lemaux[3], P. Cassata[18], V. Le Brun[3], L. Pentericci[4], L. A. M. Tasca[3], E. Vanzella[2], E. Zucca[2], R. Amorín[4], S. Bardelli[2], M. Castellano[4], A. Cimatti[5], O. Cucciati[5,2], A. Durkalec[3], A. Fontana[4], M. Giavalisco[13], A. Grazian[4], N. P. Hathi[3], O. Ilbert[3], S. Paltani[9], B. Ribeiro[3], V. Sommariva[5,4], M. Talia[5], L. Tresse[3], D. Vergani[6,2], P. Capak[12], S. Charlot[7], T. Contini[8], S. de la Torre[3], J. Dunlop[16], S. Fotopoulou[9], L. Guaita[4], A. Koekemoer[17], C. López-Sanjuan[11], Y. Mellier[7], J. Pforr[3], M. Salvato[14], N. Scoville[12], Y. Taniguchi[15], and P. W. Wang[3]

(Affiliations can be found after the references)

ABSTRACT

We investigate the effect of different star formation histories (SFHs) on the relation between stellar mass (M_*) and star formation rate (SFR) using a sample of galaxies with reliable spectroscopic redshift $z_{\rm spec} > 2$ drawn from the VIMOS Ultra-Deep Survey (VUDS). We produce an extensive database of dusty model galaxies, calculated starting from a new library of single stellar population (SSPs) models, weighted by a set of 28 different star formation histories based on the Schmidt function, and characterized by different ratios of the gas infall timescale $\tau_{\rm infall}$ to the star formation efficiency ν. Dust extinction and re-emission were treated by means of the radiative transfer calculation. The spectral energy distribution (SED) fitting technique was performed by using GOSSIP+, a tool able to combine both photometric and spectroscopic information to extract the best value of the physical quantities of interest, and to consider the intergalactic medium (IGM) attenuation as a free parameter. We find that the main contribution to the scatter observed in the *SFR-M*$_*$ plane is the possibility of choosing between different families of SFHs in the SED fitting procedure, while the redshift range plays a minor role. The majority of the galaxies, at all cosmic times, are best fit by models with SFHs characterized by a high $\tau_{\rm infall}/\nu$ ratio. We discuss the reliability of a low percentage of dusty and highly star-forming galaxies in the context of their detection in the far infrared (FIR).

Key words. galaxies: evolution – galaxies: formation – galaxies: high-redshift – galaxies: star formation

1. Introduction

A fundamental observable in astrophysical cosmology is the cosmic history of star formation. In a recent review, Madau & Dickinson (2014) noted that not only it is still hard to accurately determine the redshift of the highest star formation rate density (SFRD), but that beyond redshift ∼2 there is considerable uncertainty in the amount of stellar light obscured by dust. To this, we can add the uncertainties in deriving stellar masses and star formation rates (SFRs) for large complete samples of galaxies with well-known selection functions. Specifically, reliable indicators of the SFR, like the Hα flux, are redshifted into the K band or beyond at $z > 2$, where spectrographs do not yet allow large samples to be collected. Other indicators, like the far-infrared (FIR) luminosity, are limited to the brightest population because of the sensitivity of *Herschel* (Lemaux et al. 2014; Rodighiero et al. 2014). In the past years there have been some developments in terms of estimating SFRs on composite or individual galaxies at higher redshift through *Herschel* stacking (Álvarez-Márquez et al. 2016), through color evolution and estimating equivalent-widths of recombination lines with broadband photometry (Faisst et al. 2016), VLA/ALMA observations of galaxies that are star-forming at relatively normal levels, and larger samples of KMOS/MOSFIRE H$_\alpha$/H$_\beta$/[OII] emitters, to mention only a few examples. But still, astronomers must rely on fitting the galaxy spectral energy distributions (SEDs) with galaxy models that imply, by nature, some assumptions on several galaxy properties, including their stellar initial mass function (IMF), the chemical composition and its evolution, the dust-attenuation law, and the star formation histories (SFHs). Uncertainties in the underlying single stellar populations models, SSPs, also affect the estimate of the energy output of the stellar populations, mostly because of the contribution of stars of low and intermediate mass experiencing the thermally pulsing asymptotic giant branch phase (TP-AGB; Maraston et al. 2006; Cassarà et al. 2013; Villaume et al. 2015). Several authors have addressed the way in which different assumptions can influence the SED-fitting results: for instance, Papovich et al. (2001) and Conroy et al. (2009) have investigated the effect of the IMF, Conroy et al. (2009) have also studied the effect of metallicity evolution, and Maraston et al. (2006) the effect of stellar evolution models. For a detailed review on these issues, we refer to Conroy (2013).

Notwithstanding these limitations, the comparison of the broadband spectral energy distribution of galaxies with that of a population of stars with given IMF, SFH, age, dust reddening, and metallicity remains one of the most widely used methods to infer the physical properties of galaxies over a wide redshift range (Sawicki & Yee 1998; Papovich et al. 2001; Guo et al. 2012, to mention only a few). When modeling the SED of galaxies, some parametrization of the SFH must be used (Ilbert et al. 2010; Lee et al. 2010; Wuyts et al. 2011; Ilbert et al. 2013). The SFH can in principle be arbitrarily complex, but simple forms are often adopted: one frequently used form is

a declining exponential model, where $SFH \propto \exp(-t/\tau)$, as would be predicted from a closed-box model of galaxy evolution (Schmidt 1959; Tinsley 1980). It is worth recalling that the closed-box model of galaxy evolution, applied to study the chemical history of the solar neighborhood, fails to explain the metallicity distribution observed among old field stars, giving rise to the so-called G-dwarf problem. Models with infall are able to solve this problem because they avoid the excess of very low-metal stars: the metallicity increases faster, and a few stars are formed at very low metallicities (Chiosi 1980; Bressan et al. 1994; Pipino et al. 2013). However, the use of exponentially declining SFH reproduces the optical/near IR colors of local spiral galaxies (Bell & de Jong 2000) and the global evolution in the SFRD for $z < 2$ (Nagamine 2000).

During the past decades, the advent of high-redshift surveys has enabled identifying and studying very many high-redshift galaxies (Davis et al. 2003; Steidel et al. 2003; Ouchi et al. 2008; Vanzella et al. 2009; Kashikawa et al. 2011; Bielby et al. 2013; Le Fèvre et al. 2005, 2013), and contemporaneous studies from hydrodynamical simulations and semianalytic models (Finlator et al. 2007, 2011) have suggested the need for rising star formation histories when studying the properties of galaxies at $z > 2$. Finkelstein et al. (2010) and Papovich et al. (2011) required rising star formation histories (at least on average) to explain the evolution of the ultraviolect (UV) luminosity function. The SFRs and stellar masses for galaxies at $z > 2$ appear inconsistent with their having formed stars following an exponentially declining or constant star formation history before the epoch during which they are observed (Reddy et al. 2012). Lee et al. (2009) analyzed the SEDs of high-z theoretical galaxies and concluded that the use of a single exponentially decreasing SFH underestimates SFRs and overestimates ages by a factor of ∼2 in both cases: subsequent works (Lee et al. 2010; Maraston et al. 2010; Wuyts et al. 2011) confirmed this result and concluded that models with rising SFHs provided a better fit to high-z SEDs and produce SFRs in better agreements with other indicators. Models with rising star formation histories in general lead to high SFRs, since their SED is always dominated by young stars, which implies a narrower range of UV to optical fluxes, on average requiring a higher dust attenuation than for other SFHs (Schaerer & Pelló 2005).

There are different opinions regarding which functional form should be adopted for rising SFHs. Maraston et al. (2010) and Pforr et al. (2012) advocated exponentially increasing SFHs, while Lee et al. (2010) suggested the use of delayed τ models ($SFH \propto t \times \exp(-t/\tau)$). The data do not favor one functional form over the other, and the basic conclusion is that the model SFH library must be sufficiently diverse to allow for a wide range in SFH types (Conroy 2013), especially when studying galaxies at high redshift, where many uncertainties still hold. One of the main arguments often invoked to support rising star formation histories is the small scatter in the SFR-M_* relation (Schaerer et al. 2013).

Up to $z \sim 2$, the correlation between star formation rate and stellar mass of galaxies, and its evolution with redshift, has been extensively studied in the past years by many authors (e.g., Daddi et al. 2007; Elbaz et al. 2007; Rodighiero et al. 2011): the galaxies following this relation define what has been called the main sequence of star-forming galaxies (SFGs; Noeske et al. 2007).

The slope and the scatter of this relation together with its evolution in redshift set constraints on the SFHs of galaxies as a function of their mass (Buat et al. 2012). It is worth underlining that the SFR is generally derived from observables (UV and IR luminosity) that depend on timescales $t \gtrsim 100$ Myr and are assumed to be in an equilibrium value, which is only reached after this timescale and for constant SFR. The consequence of these assumptions entering the SFR(UV) or SFR(IR) calibrations (Kennicutt 1998) is that the observational scatter is smaller than the true scatter in the current SFR when typical ages are younger than 100 Myr or for shorter timescales, which is especially true at high redshift (Schaerer et al. 2013). Schaerer et al. (2013) and de Barros et al. (2014) showed that the idea of a simple, well-defined star-forming sequence with the majority of SFGs showing a tight relation between stellar mass and SFR suggested by studies at low redshift ($z \leq 2$, Daddi et al. 2007; Elbaz et al. 2007; Noeske et al. 2007) may not be appropriate at high redshift. A relatively small scatter is only obtained assuming star formation histories to be constant over long timescales ($t \gtrsim 50$ Myr), while a significant scatter is obtained for models assuming rising or delayed star formation histories, which are often suggested in recent works.

Tasca et al. (2015) recently presented a study on the evolution with redshift of the SFR-M_* relation and of the sSFR of a sample of 4531 galaxies from the VUDS survey, with spectroscopic redshifts between 2 and 6.5. The values of M_* and SFR have been obtained by fitting all the available multiwavelength data with Le Phare code (Arnouts et al. 1999; Ilbert et al. 2006) and using a range of templates coming from the Bruzual & Charlot (2003) models. The assumed IMF is the Chabrier IMF, while the adopted SFHs are exponentially declining ($SFR \propto e^{-t/\tau}$) and two delayed SFHs models with peaks at 1 and 3 Gyr. The authors concluded that the $\log SFR - \log M$ relation for SFGs remains linear up to $z = 5$ but the SFR increases at a fixed mass with increasing redshift. For stellar masses $M_* \geq 10^{10}\ M_\odot$ the SFR increases by a factor 1.7 from redshift $z \sim 2.3$ up to $z \sim 4.8$.

In this paper we aim at measuring the stellar mass and the SFR using different assumptions about star formation histories to investigate the nature of the scatter of SFR-M_* relation. We use a sample of 2995 VUDS galaxies with reliable spectroscopic redshift $z_{\rm spec} > 2$ (Le Fèvre et al. 2015). The SED fitting is performed using the photometric data, the spectra, a new set of galaxy models built from SSPs recently developed by Cassarà et al. (2013), and an ample choice of SFHs, described in Appendices A and B. The treatment of the dust absorption and re-emission is based on the radiative transfer model. The plan of the paper is the following: in Sect. 2 we describe the properties of the galaxy sample and in Sect. 3 the galaxy models and the allowed range of free parameters. In Sect. 4 we show the results of a test on a set of mock galaxies to validate the use of the galaxy models. In Sect. 5 we present the SED fitting tool and procedure, while in Sect. 6 we present the results, which are discussed in Sect. 7. Section 8 is devoted to a short summary. We assume a cosmology with $\Omega_{\rm m} = 0.27$, $\Omega_\Lambda = 0.73$ and $H_0 = 70.5\ {\rm km\,s^{-1}\,Mpc^{-1}}$.

2. VUDS sample

The VIsible MultiObject Spectrograph (VIMOS) Ultra Deep Survey (VUDS, Le Fèvre et al. 2015) is a spectroscopic redshift survey devised to study galaxy evolution in the high-redshift Universe, taking advantage of the multiplexing capabilities of VIMOS on the VLT (Very Large Telescope array). This analysis is based on a subsample of the 7843 galaxy redshifts measured in three separate fields (COSMOS, VVDS-02h, and ECDFS) where ample photometric data are also available.

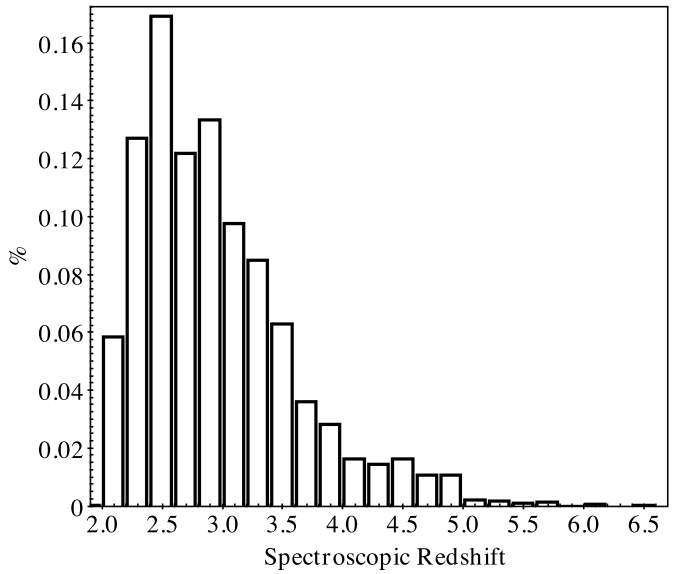

Fig. 1. Normalized redshift distribution of VUDS galaxies used in this study.

As reported in Tasca et al. (2015), each of the fields has multiband photometry covering at least from broadband u to *Spitzer*-IRAC 4.5 μm. The COSMOS field has the most extensive photometric set composed of more than 30 bands, including standard broadband and medium-band photometry (Laigle et al. 2016). The broadband photometric databases of VVDS-02h and ECDFS have been presented in Le Fèvre et al. (2015) and Cardamone et al. (2010), respectively. VUDS targets have mainly been selected on the basis of their photometric redshifts, requiring that either the first or second peak in the photometric redshift probability distribution satisfy the condition $z_{\rm phot} + 1\sigma \geq 2.4$ and $i_{\rm AB} \leq 25$. Exposure times were 14h with both the VIMOS blue and red low-resolution grisms with slits one arcsecond wide. The blue and red parts of the spectra were normalized in the common wavelength range and joined together to obtain a spectrum covering from 3650 to 9350 Å.

Redshifts were measured independently by two astronomers and disagreements were discussed before assigning them a confidence level.

For this work we selected all objects with $z_{\rm spec} \geq 2$ and a confidence level >75%, that is, with flags 2, 3, 4, and 9 (see Le Fèvre et al. 2015, for more details about the redshift measurement and the survey in general). These requirements are satisfied by 3948 VUDS galaxies (1994 in the COSMOS field, 1499 in the VVDS-02h, and 455 in the ECDFS field). The SED fitting was performed considering all the available broad- and medium-band photometric data.

Figure 1 shows their redshift distribution: 61% of the galaxies have $2 < z_{\rm spec} < 3$, 31% have $3 < z_{\rm spec} < 4$, while only 8% have $z_{\rm spec} > 4$. The redshift range is $2.00 < z_{\rm spec} < 6.54$, while the mean and median value are $z_{\rm spec,mean} = 2.96$ and $z_{\rm spec,median} = 2.83$, respectively.

3. Galaxy models

The SED fitting was performed using a large database of dusty model galaxies (about 30 000 evolutionary models) obtained by varying the physical input parameters. The galactic models were calculated starting from the extended library of isochrones and SSPs of different chemical compositions and ages. The definition of age throughout the paper means the time passed since the first stars started forming in a galaxy. In the models we took into account a new treatment of the TP-AGB phase including the effect of circumstellar dust shells around AGB stars (Cassarà et al. 2013). Even though the AGB phase is short lived, the AGB stars are very bright, can reach very low effective temperatures, and easily become enshrouded in a shell of self-produced dust that reprocesses the radiation from the underlying stars. AGB stars have a non-negligible effect on the rest frame near-IR spectra of galaxies and can significantly alter the M_*/L ratio of intermediate-age populations. The contribution of the TP-AGB stars is limited to galaxies dominated by stars with ages in the range 0.3−2 Gyr, depending on metallicity (Maraston 2005; Bruzual 2007; Marigo et al. 2008). At $z \sim 2.5$, a sizable fraction of the stellar populations has mean ages in the range 0.5−1.5 Gyr, which means that it is mostly affected by the TP-AGB stars (Zibetti et al. 2012), and even accounting for the high uncertainty affecting the theoretical modeling of this phase, stellar population models including the TP-AGB stars allow for a better determination of galaxy ages and hence stellar masses. These are fundamental quantities for studying galaxy formation and evolution (Maraston et al. 2006). From these brief considerations, the correct inclusion of a more realistic modeling of the TP-AGB phase in SSPs and hence galaxy models appears not negligible, both for studies in the local Universe and at high redshifts.

A physically realistic coupling between the populations of stars and the effect of attenuation and emission by dust is critical to determine the properties of galaxies: see Appendix A for more details about the SSPs and for the treatment of dust extinction and re-emission, and Appendix B for the features of the composite stellar populations (CSPs). The models do not include the contribution of the emission lines: their net effect in the derivation of stellar masses and SFRs has been explored by many authors: in our redshift range, the SED-derived masses could change by 0.1−0.2 dex (Ilbert et al. 2009; de Barros et al. 2014; Salmon et al. 2015; Tasca et al. 2015), even though according to Salmon et al. (2015) this may affect about 65% of the galaxies. We used the Schmidt law (Schmidt 1959) for the star formation rate, which in the formalism of adopted chemical evolution models (see Appendix A) becomes

$$SFR(t) = \nu M_{\rm g}(t)^k, \tag{1}$$

where $M_{\rm g}$ is the mass of the gas at the time t, k yields the dependence of the star formation rate on the gas content, while the factor ν measures the efficiency of the star formation process. Because of the competition between the gas infall, gas consumption by star formation, and gas ejection by dying stars, the SFR starts very low in this type of models, grows to a maximum and then declines. The functional form that could mimic the trend for the gas infall prescription is a delayed exponentially declining law $t \times \exp(-t/\tau)$. The timescale $\tau_{\rm infall}$ roughly corresponds to the age at which the star formation activity reaches the peak value (see Appendix A). The shape of star formation rate is mostly driven by the two aforementioned parameters $\tau_{\rm infall}$ and ν. The final interplay between them drives its evolution with time (see Fig. 2). The complete formalism of the chemical evolution models can be found in its original form in Tantalo et al. (1996) and Portinari & Chiosi (2000), while a short summary is provided in Cassarà et al. (2015). With this law for the star formation, we are able to model two main types of objects: the first type of models are what we call bulge-like models, characterized by high values

Table 1. Input parameters for SED fitting with GOSSIP+.

SSPs	Range
Metallicities	0.0004, 0.004, 0.008, 0.02, 0.05
Ages	0.03−3 Gyr
Optical depths in the V band τ_V	0.01, 0.03, 0.05, 0.08, 0.1, 0.3, 0.5, 0.8, 1, 1.3, 1.5, 1.8, 2, 2.3, 2.5, 2.8, 3, 3.3, 3.5, 4
IMF	**Range**
Salpeter law	0.1−100 $M_\odot$
ζ	0.35−0.39−0.50
Slope	−2.35
SFHs	**Range**
Infall time $\tau_{\rm infall}$	5−0.30 Gyr
Efficiency of the SF ν	14−0.35
Exponent of the Schmidt function k	1
IGM transmission	19% to 100% at $z_{\rm spec}$ = 3.0
(seven possibilities at any $z_{\rm spec}$)	5% to 50% at $z_{\rm spec}$ = 5.0

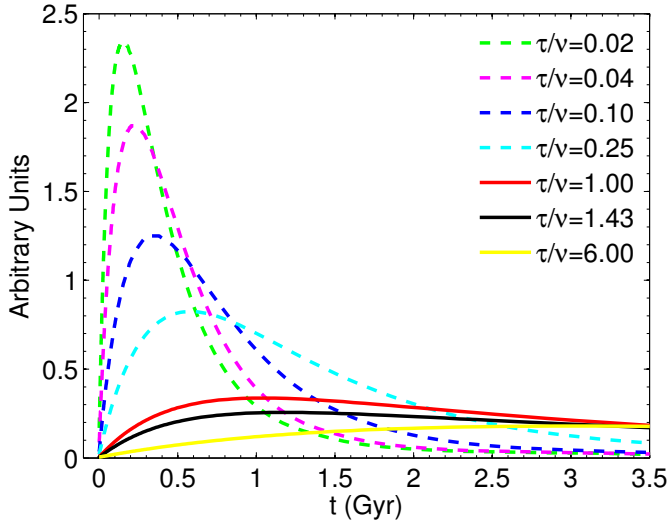

Fig. 2. Evolution with time of the seven main families of the SFHs used in this work. Dashed and solid lines represent SFHs typical for bulge- and disk-like models, respectively.

of ν and low values of $\tau_{\rm infall}$, with a rapid rise of the star formation rates, a peak reached on a relatively short timescale (on average 0.5 Gyr), and a declining phase. These models reproduce the chemical pattern in the gas of elliptical galaxies at both low (Piovan et al. 2006b; Pipino & Matteucci 2011) and high redshift (e.g., Matteucci & Pipino 2002; Pipino & Matteucci 2011). The second type of models are what we call disk-like models, characterized by low values of ν, together with high values of $\tau_{\rm infall}$, which show a slow rising and declining SFR: they reproduce disk galaxies in the local Universe (Piovan et al. 2006b; Pipino et al. 2013).

Many prescriptions for the SFHs can be found in the literature: our choice of using a variety of SFHs and not the classical $\propto e^{(t/\tau)}$ is based on the following reasons. As amply described in Appendix B, model galaxies are typically obtained considering a convolution of SSPs of different age and metallicity, weighted by the SFHs: in our case, we also considered the chemical enrichment that is described by the infall model (Chiosi 1980; Pipino et al. 2013). In this framework, the Schmidt function is a physical prescription that relates the gas content to the star formation activity, allowing us to model different types of objects by varying their parameters (Buzzoni 2002).

The original catalog of 28 different SFHs (see Table B.1) can be grouped into seven families shown in Fig. 2, according to the increasing ratio between $\tau_{\rm infall}$ and the efficiency of the star formation rate ν. This ratio is in turn representative of the two populations of model galaxies, bulge-like (dashed lines in Fig. 2) and disk-like (solid line in Fig. 2). Table 1 gives the range of free parameters for the dusty SSPs, the galaxy models, the SFHs, and the IGM transmission. We recall that each combination of $\tau_{\rm infall}$, ν and ζ (Table B.1) gives rise to 28 sets of evolutionary galaxy models. ζ describes the fraction of total mass in form of stars stored in the IMF above a given mass M_*, which is the minimum mass contributing to the nucleosynthetic enrichment of the ISM over a timescale on the order of the galaxy life (Bressan et al. 1994; Tantalo et al. 1996; Cassarà et al. 2015). This is equivalent to fixing the lower limit of the integral on the SSP mass used to normalize the IMF. While the upper limit of the integral could be fixed to 100 or 120 $M_\odot$ because massive stars are a small fraction of a stellar population defined with a Salpeter IMF, the lower mass stars have a higher contribution to the SSP global mass, but not to its luminosity. Therefore, adopting a lower limit for the IMF (e.g., 0.01 $M_\odot$) instead of 0.1 $M_\odot$ can lead to more low-mass stars and create a stellar population less luminous (in mass unity) and with a reduced capability of enriching the ISM (see Bressan et al. 1994; Tantalo et al. 1996; Portinari & Chiosi 1999; Piovan et al. 2011; Cassarà 2012; Cassarà et al. 2015 for an extensive discussion on this topic). Following the suggestion of Tantalo et al. (1996), Portinari et al. (2004) and Cassarà (2012), we adopted three values for ζ for our models, namely 0.35, 0.39, and 0.50.

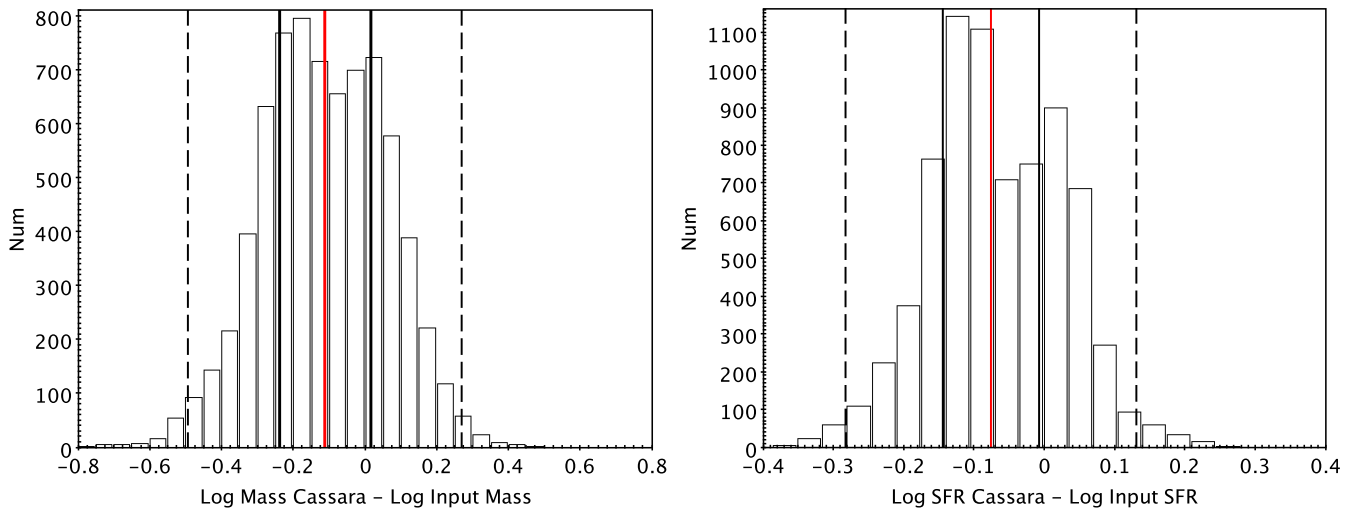

Fig. 3. *Left panel*: distribution of the differences between the values of stellar mass inferred from SED fitting on the mock galaxies and the input values. The red solid line is the median. Black dashed and solid lines indicate three and one times the median absolute deviation (MAD), respectively. *Right panel*: as in the left panel, but for the values of SFRs.

The galaxy models were calculated by varying the possible values of the optical depth τ_V, and hence of the database of dusty SSPs. It is worth underlining the relation between τ_V and A_v: $A_v = 1.086 \times \tau_V$ (more details in Appendix A.1).

4. Validation of the models: test with mock galaxies

We performed a test on a set of mock galaxies to inspect the capability of our models to recover the input values of stellar masses and SFRs. The mock galaxies were based on galaxy models from the PEGASE library (Fioc & Rocca-Volmerange 1997). The use of this library is justified by the self-consistent treatment of the evolution of galaxy physical properties, without the need of fixing and choosing the metallicity and extinction of the populations, for example, as in Bruzual & Charlot (2003) models. These models do not adopt the same SSPs used in this paper and have a different approach for the dust extinction. The IMF for the mock sample was the Salpeter law integrated between two fixed values (Fioc & Rocca-Volmerange 1997). These models are characterized by ages ranging from 0.1 to 2.5 Gyr and timescales of star formation histories between 0.1 and 7 Gyr. These choices lead to models with star formation histories that can be exponentially declining, constant, or delayed exponential, depending on the combinations of their age and timescale. The final sample of synthetic models comprised 7350 galaxies, with stellar masses between 10^8 and 10^{12} $M_\odot$ and SFRs between 1 and 200 $M_\odot$/yr, following the main sequence at $z = 2$ as defined by Daddi et al. (2007), with a slope of $\alpha = 0.87$. The SED of the mock galaxies had photometry from the u band to the IRAC 4.5 μm band (the longer wavelength that can be simulated using this library to create mock galaxies), and their simulated spectra covered a spectral range from 3500 to 9600 Å with an average $S/N \sim 3.5$. VUDS galaxies reach a $S/N = 5$ on the continuum at 8500 Å for $i_{AB} = 25$ (Le Fèvre et al. 2015). The photometric data come with random errors, while spectra were computed by adding realistic noise spectra.

We used GOSSIP+ (see below) to fit the mock galaxy SEDs with our models, and the results of this exercise are shown in the panels of Fig. 3. The distribution of the differences between the values inferred from the SED fitting using the set of models presented in this paper and the input values of PEGASE mock galaxies for the stellar masses is shown in the left panel of Fig. 3. The median value of the differences is −0.11 dex (red line in the left panel of Fig. 3), with 1 median absolute deviation (MAD) of 0.12 dex (black solid lines in the same panel). The dotted lines show three times the MAD. Stellar mass is considered as the most reliable parameter estimated by SED fitting, since relatively small differences are found while varying the assumptions for the star formation histories and/or the dust extinction. Finlator et al. (2007) estimated that differences due to different assumptions on SFHs are around 0.30 dex, and Yabe et al. (2009), adding effects of metallicity and extinction law, estimated differences not higher than 0.60 dex.

The distribution of the differences between the SFRs as inferred from GOSSIP+ with respect to input SFRs presents a median value of −0.07 dex (red line in the right panel of Fig. 3) with 1 MAD of 0.06 dex (black solid lines in the same panel). The dotted lines indicate the 3 MAD dispersion.

We note a slight bimodality in both panels of Fig. 3. A significant number of galaxies presents differences in SFRs between −0.07 dex and −0.13 dex (left peak in the histogram, right panel of Fig. 3), while a smaller percentage presents differences in SFRs between 0 and 0.05 dex (right peak in the same histogram). This feature also appears in the left panel of Fig. 3, but not as strong as in the right panel. The driver of this bimodality is the adoption of different values of ζ with respect to the single value allowed for the mock galaxies. This bimodality is not observed in any of the following plots presenting the results of the SED fitting on the VUDS galaxies. None of the physical properties shows any correlations with the values of ζ.

These differences in stellar mass and SFR estimates are fully acceptable, taking into account the uncertainties coming from the adoption of the SED fitting technique (Conroy 2013). From the tests we performed and the above discussion, we can conclude that the template library we used features a sufficiently broad range of SFHs and extinctions to encompass those in the PEGASE library and that the SED fitting works properly. We

can confidently use the galaxy models to recover the physical properties of the VUDS galaxies.

5. SED fitting tool and procedure

We made use of GOSSIP+ (galaxy observed-simulated SED interactive program), a spectral/SED fitting software. It has been developed by the PANDORA group at INAF-IASF Milano (Franzetti et al. 2008) and was partially modified and completed at LAM in Marseille. The full description of the new version of the software is presented in Thomas et al. (2016): for the sake of clarity, here we briefly summarize its capabilities. GOSSIP+ is a software that is able to combine the spectroscopic information with the photometric data points. One main improvement implemented in GOSSIP+ deals with the IGM attenuation. Most current SED fitting softwares use the Madau prescription (Madau 1995). This means that for a given redshift a single extinction curve is considered, while GOSSIP+ allows choosing among seven IGM extinction curves at any redshift. To account for the vastly different number of spectral data points with respect to the photometric data points, a combined χ^2 is computed by GOSSIP+ as the sum of the reduced χ^2 of the photometric and of the spectrum data fit to evaluate the two different data sets with the same weight. For the sum of two reduced χ^2 we adopted as a definition of a total reduced χ^2 the following: $\chi^2_{\rm red} = 0.5(\chi^2_{\rm phot} + \chi^2_{\rm spec})$. As for the prominent emission lines in the spectra, GOSSIP+ gives the possibility of defining some avoidance regions of the spectra (which are then redshifted to each object redshift) that will be avoided in the fitting procedure.

Stellar masses, SFRs, dust absorption, age and metallicity of the stellar populations, UV luminosity and level of IGM extinction are obtained simultaneously employing a χ^2 minimization to find the best-fit model considering the age of the Universe at the observed redshift as an upper limit for the choice of the models. The agreement between spectroscopy and photometry is crucial to produce a good fit. As discussed in Thomas et al. (2016), a mismatch between these two datasets occasionally occurs, and this affects the quality of fit. Thomas et al. (2016) performed a visual inspection to define the quality of the fit. We decided to select the final sample of galaxies in the following way: as a first step, we excluded galaxies with values of the total reduced $\chi^2_{\rm red} > 5$, and as a second step, we excluded galaxies with values of reduced photometric $\chi^2_{\rm phot} > 5$. Finally, a visual inspection of the excluded galaxies confirmed that in this way we retained only galaxies with a reliable fit. High values of χ^2 are almost always due to a very reduced set of photometric data and/or a spectrum with low S/N, and thus the physical properties that can be inferred could be highly uncertain. The $\chi^2_{\rm red}$ distribution of the 2995 galaxies is shown in Fig. 4, while Fig. 5 shows the results of the fitting procedure for four galaxies at different redshifts. The final sample comprises 2995 galaxies (1737 in the COSMOS field, 1005 in the VVDS-02h and 253 in the ECDFS field) with reliable spectroscopic redshift between 2.00 and 6.54.

6. SED fitting results

We here investigate the change in the *SFR*-M_* relation when the SED fitting is performed with a set of models with different SFHs. Figure 6 shows the outcome of our SED fitting procedure on 2995 VUDS galaxies spanning a wide range of redshifts. The spread in SFRs for a given stellar mass is quite strong (on the order of 1 dex), and there is a suggestion of two distinct main sequences showing SFRs differing by 0.6 dex, plus a population of highly SFGs amounting to 5% of the sample.

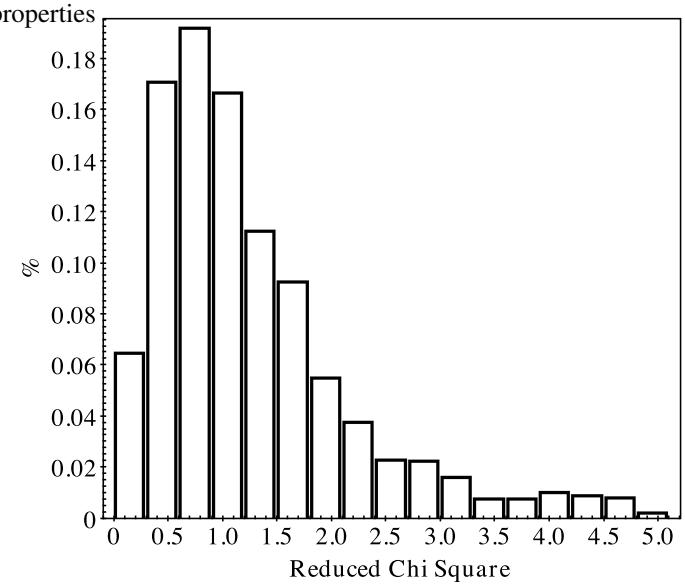

Fig. 4. Normalized distribution of the object sample with $\chi^2 < 5$.

The spread in SFRs might either be due to the wide redshift range covered by the VUDS galaxies because of the evolution of the *SFR*-M_* relation between $z \sim 5$ and $z \sim 2$ (Elbaz et al. 2007; Fumagalli et al. 2014; Tasca et al. 2015), or to the use of different star formation histories (Salmon et al. 2015). To separate these two effects, we divided our sample into redshift bins and according to the type of SFHs of the best-fit model. For the redshift, we subdivide the sample into three redshift bins of approximately 570 Myr ($2.00 \leq z_{\rm spec} < 2.42$, $2.42 \leq z_{\rm spec} < 3.03$, and $3.03 \leq z_{\rm spec} < 4.00$) and the fourth one including all galaxies with $z_{\rm spec} \geq 4.00$. For the SFHs, we considered three different families: (a) $\rm SFH_{con}$ characterized by low star formation efficiency ν and high values of the infall timescale $\tau_{\rm infall}$ (shown with solid curves in Fig. 2); (b) $\rm SFH_{ris}$ characterized by high star formation efficiency and low gas infall timescales (dashed lines in Fig. 2, rising part); (c) $\rm SFH_{dec}$: again, they present high values for the star formation efficiency and low gas infall timescales (dashed lines in Fig. 2, declining part).

The three panels of Fig. 7 show the *SFR*-M_* plane for the three groups of SFHs, where galaxies were color coded according to the redshift bins. It is worth underlining that each panel is populated by galaxies of different redshift range. The left panel shows that a classical main sequence arises from galaxies fit by models with $\rm SFH_{con}$, while galaxies best fit by models with rising SFHs $\rm SFH_{ris}$ define a second main sequence with higher sSFR (Fig. 7, central panel) and, on average, younger ages. Finally, the right panel of Fig. 7 shows galaxies fit by models with declining SFHs $\rm SFH_{dec}$. This last group of galaxies shows higher masses than the others, moderate SFRs, and older ages (see Fig. 8). No clear main sequence is visible in this last group.

The panels of Fig. 9 show the *SFR*-M_* plane for galaxies divided into the four redshift bins. It is clearly visibile that all redshift bins show a similar scatter that is due to the presence of galaxies fitted by models with different SFHs. Figures 7 and 9 show that redshift is not the dominant factor for the spread observed in the *SFR*-M_* plane.

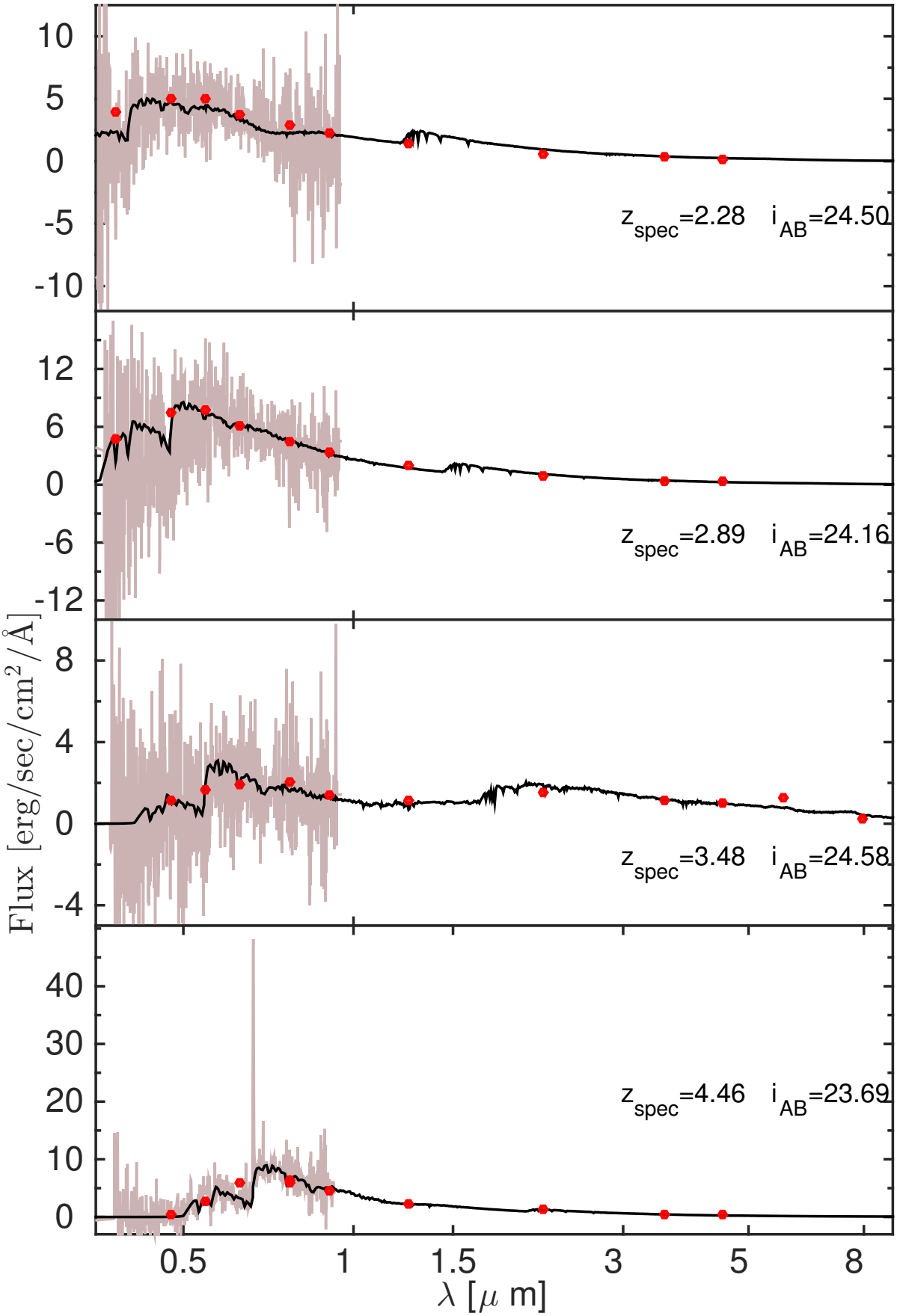

Fig. 5. Examples of model fits to the data using GOSSIP+. The dark curve represents the best-fitting model, the gray curve the spectra, and the red points are the photometric determinations. Fluxes are given in units of 10^{19} [erg/s/cm^2/Å]. The redshifts and the $i_{\rm AB}$ of the objects are shown in each panel.

Table 2. Redshift evolution for galaxies with different star formation histories.

SFH/Δ z_{spec}	$2.00 \leq z_{spec} < 2.42$	$2.42 \leq z_{spec} < 3.03$	$3.03 \leq z_{spec} < 4.00$	$z_{spec} \geq 4.00$
SFH_{con}	417 (68%)	893 (65%)	437 (52%)	75 (49%)
SFH_{ris}	96 (16%)	351 (27%)	272 (32%)	41 (26%)
SFH_{dec}	97 (16%)	112 (8%)	143 (16%)	38 (25%)

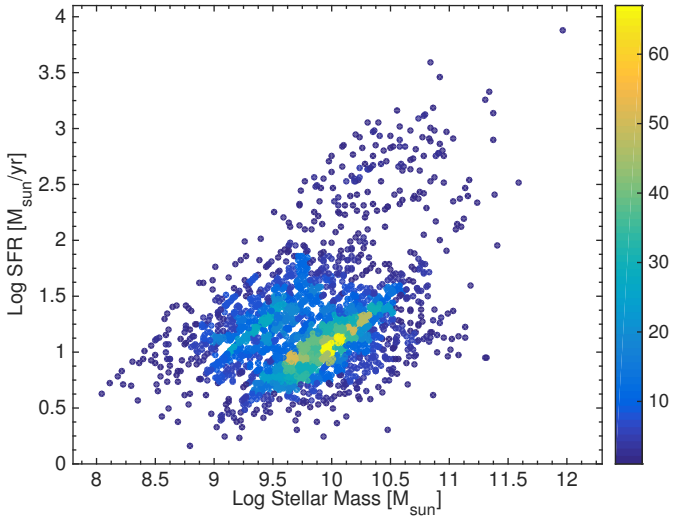

Fig. 6. *SFR-M_** density map for the complete sample of VUDS galaxies.

We furthermore note that the proportion of galaxies fit by the models with different SFHs changes with the age of the Universe. Galaxies occupying the classical main sequence (SFH_{con}, blue points) increase from about 50% to 68% as the Universe ages, while the more rapidly SFGs (SFH_{ris}, red points) decrease from about 30 to 15−20%, as shown in Fig. 10 and Table 2. The last point we would like to note is that those galaxies showing the highest SFRs (greater than 100 $M_\odot$/yr) and representing 5% of the sample have higher optical depths.

7. Discussion and conclusions

When used to fit the SEDs of high-redshift SFGs, our set of models including SFHs of different shapes produces an *SFR-M_** relation showing a broad spread. We have shown that this broad spread is not due so much to the wide redshift range, but to the different SFHs used. This implies that the dominant stellar populations of galaxies of similar mass can have substantially different ages and also quite different sSFRs. We could interpret the bimodal appearance of the *SFR-M_** relation as due only to the limited number of models we used for the SED fitting, that is, the discreteness of the combination of the ν and τ_{infall} parameters. A more extended model library with a less discrete parametrization of ν and τ_{infall} could, in principle, show a more continuous distribution of galaxies in the *SFR-M_** plane. Nonetheless, some evidence of a bimodal *SFR-M_** relation has been discussed in Bernhard et al. (2014). The analysis of Fig. 10 underlines that galaxies fitted by models that adopt SFH_{con}, for instance, showing a smoother increase of the SFR than the SFR_{ris} and SFH_{dec}, represent the majority of the objects at any cosmic time. At early times their percentage decreases and the differences between the three families become less pronounced. This suggests that it is important to allow different types of SFHs, particularly at higher redshift.

Thirteen percent of our sample is made of galaxies fit by models with declining SFH and thus high star-forming efficiency and low infall timescale (SFH_{dec}, green points). These objects have a history of rapid mass build-up followed by a fast declining phase of star formation and might be the progenitors of quiescent, massive galaxies. These galaxies show, on average, a small amount of dust content and older ages, when compared to galaxies fit by SFH_{ris}.

Another interesting result is that some galaxies show high SFR and dust attenuation, which was not evident in Tasca et al. (2015), also based on the VUDS sample. The reason might be that in this paper we allowed extinctions up to $\sim A_V = 4$, while in Tasca et al. (2015) the highest extinction allowed corresponds to an A_V lower than 2 ($E(B-V) = 0.5$). It is not surprising that we find these highly SFGs: objects for which the SFR is estimated to be >100 $M_\odot$/yr have, for instance, been detected in the sub-mm or mm bands (e.g., Toft et al. 2014). At $z_{spec} > 3$ and $SFRs > 100$ $M_\odot$/yr we find a surface density of 0.02/arcmin^2 that can be compared with the expected density of dusty UV-selected galaxies of 0.23/arcmin^2 (Mancuso et al. 2016). However, given the complex selection function of the VUDS galaxies, we can only state that these galaxies might be reasonable candidates for observations in the sub-mm/mm bands with the caveat that the number of galaxies with high SFR increases as higher attenuations are allowed in the SED fitting procedure.

The COSMOS field has been observed by *Herschel*, and we can compare the 250 μm magnitudes estimated by the best-fit models with the observed magnitudes of the galaxies detected by *Herschel*. Figure 11 shows the distribution of the 250 μm magnitudes estimated by the SED fitting procedure. The distribution is peaked at around 19 mag with a bright and a lower fainter tail. The bright tail corresponds to galaxies with the higher SFR and shows magnitudes on the same order as those detected by *Herschel*, shown with a black solid line in Fig. 11. The inner histogram shows the zoom of the brightest region. The flux comparison shown in the histogram is statistical. The correspondence is not perfectly 1:1 because for many galaxies the SED fitting procedure shows a magnitudes fainter than the observed one. This might indicate that the *Herschel* 250μm fluxes in many cases are due to multiple components (Scudder et al. 2016).

8. Summary

We took advantage of VIMOS Ultra Deep Survey (VUDS), the largest spectroscopic survey in the redshift range $2 \leq z_{spec} < 6.54$ (Le Fèvre et al. 2015), and explored the star formation

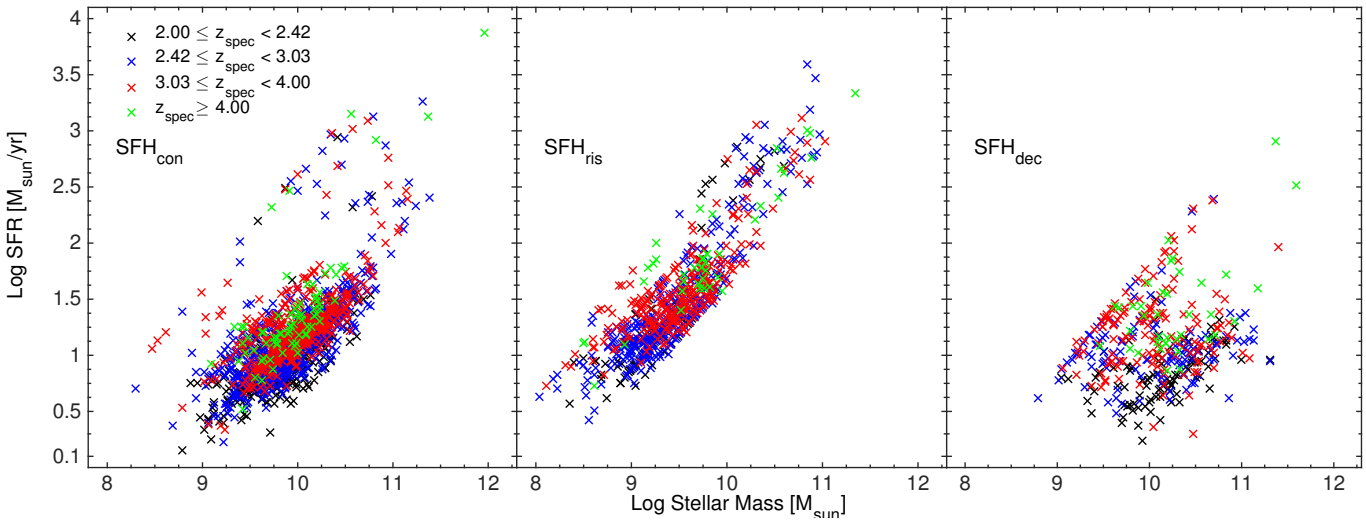

Fig. 7. *SFR-M_** plane: galaxies have been color coded according to their redshift range as the legend indicates. The *left panel* presents galaxies best fit by SFH_{con} models, in the *central panel* galaxies best fit by SFH_{ris} models, and the *right panel* galaxies best fit by SFH_{dec} models (see text for more details about these definitions).

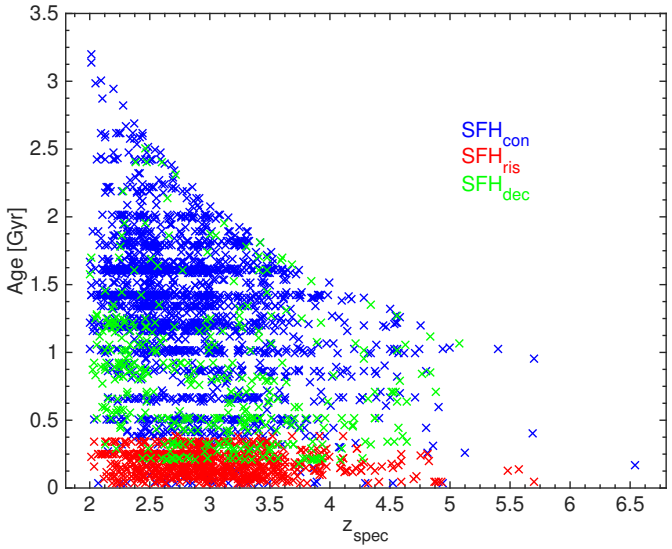

Fig. 8. Inferred values of ages as a function of redshift. Galaxies have been color coded according to their best fit SFH.

properties of 2995 galaxies with reliable spectroscopic redshifts $z_{spec} \geq 2$. The SED fitting was performed with the GOSSIP+ tool (Thomas et al. 2016), which allowed the simultaneous fitting of spectra and photometric data. As theoretical models, we built a catalog of galaxies from SSPs presented in Cassarà et al. (2013) weighted with a set of 28 different SFHs, capable of reproducing the properties of disks and bulges in the local Universe.

We focused on the relation between M_* and SFR and adopted different assumptions about star formation histories to investigate their effects on the *SFR-M_** plane and on the scatter of this relation. We found that the main cause of the scatter in the relation between stellar masses and SFRs is the contemporary adoption of different SFHs when performing the SED fitting. These results are in substantial agreement with Schaerer et al. (2013) for Lyman Break Galaxies at $z > 3$ and de Barros et al. (2014), who showed that there is a correlation between the location where a galaxy ends up in the *SFR-M_** plane and the type of SFH used in the best-fitting procedure. We obtained the same results using a variety of SFHs, which were left as free parameters for the SED fitting procedure.

The effect of the assumed forms of SFHs have been also studied by Lee et al. (2010), and their analysis has revealed that the assumption about SFHs can significantly bias the inference about stellar population parameters, in particular ages and SFRs. The recovery of the properties of galaxies by means of SED fitting process is indeed strongly influenced by the choice of the SFHs, and this can cause strong biases in the determination a posteriori of their physical properties. Currently, the data are insufficient to distinguish between simple SFHs (e.g., SFHs exponentially declining, rising and constant, SFHs that are unlikely to capture the full diversity and complexity in the SFHs in galaxies, see Reddy et al. 2012) and more complicated ones. The basic conclusion from our analysis is the importance of using a wide range of SFHs when fitting the SEDs of galaxies at high redshift to derive stellar masses and SFHs to interpret both the relation between these physical quantities and its intrinsic scatter.

Acknowledgements. The authors would like to thank the anonymous referee, whose criticism has helped to improve the quality of the manuscript. D.M. gratefully acknowledges L.A.M. hospitality during the initial phases of the project. L.P.C. acknowledges the developers of the software TOPCAT (http://www.starlink.ac.uk/topcat/). L.P.C. thanks Paolo Franzetti for his help and invaluable discussions. L.P.C. acknowledges EU FP7 funded project DustPedia. DustPedia is a collaborative focused research project supported by the European Union under the Seventh Framework Programme (2007–2013) call (proposal No. 606847), with participating institutions: Cardiff University, UK; National Observatory of Athens, Greece; Ghent University, Belgium; Université Paris Sud, France; National Institute for Astrophysics, Italy and CEA (Paris), France. This work is supported by funding from the European Research Council Advanced Grant ERC-2010-AdG-268107-EARLY and by INAF Grants PRIN 2010, PRIN 2012 and PICS 2013. A.C., O.C., M.T. and V.S. acknowledge the grant MIUR PRIN 2010–2011. This work is based on data products made available at the CESAM data center, Laboratoire d'Astrophysique de Marseille. This work partly uses observations obtained with MegaPrime/MegaCam, a joint project of CFHT and CEA/DAPNIA, at the Canada-France-Hawaii Telescope (CFHT) which is operated by the National Research Council (NRC) of Canada, the Institut National des Sciences de l'Univers of the Centre National de la Recherche Scientifique (CNRS) of France, and the University of Hawaii. This work is based in part on data products produced at TERAPIX and the Canadian Astronomy

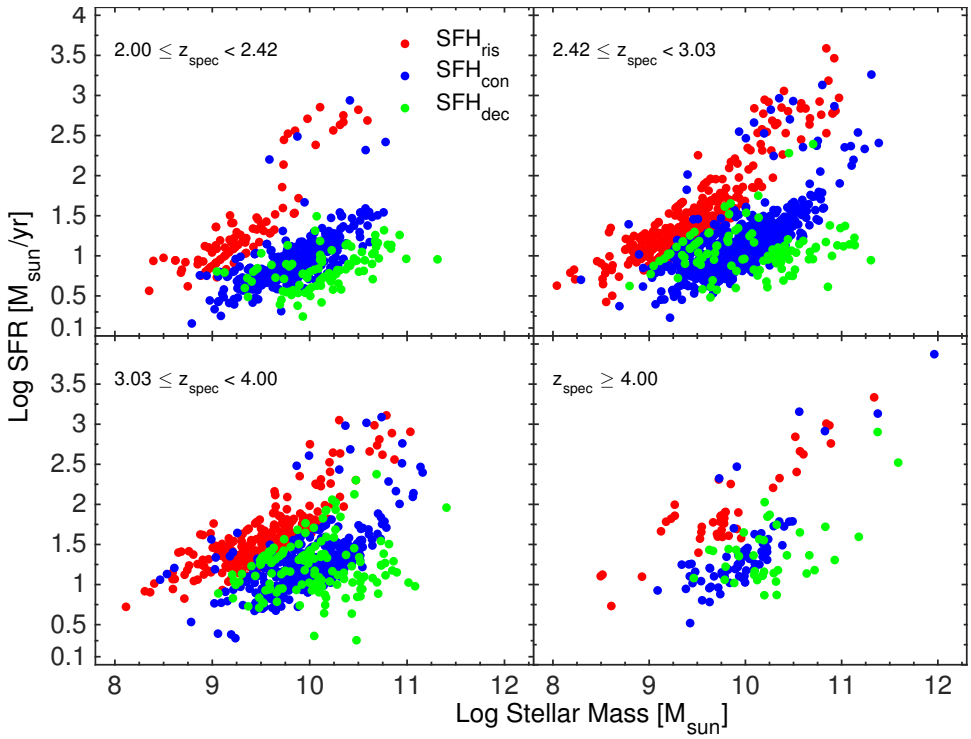

Fig. 9. *SFR-M_** plane for galaxies in the different redshift range as the legend in each panel indicates. Galaxies have been color coded according to their best-fit SFH. In blue, galaxies best fit by SFH_{con} models, in red galaxies best fit by SFH_{ris} models and in green galaxies best fit by SFH_{dec} models (see text for more details about these definitions).

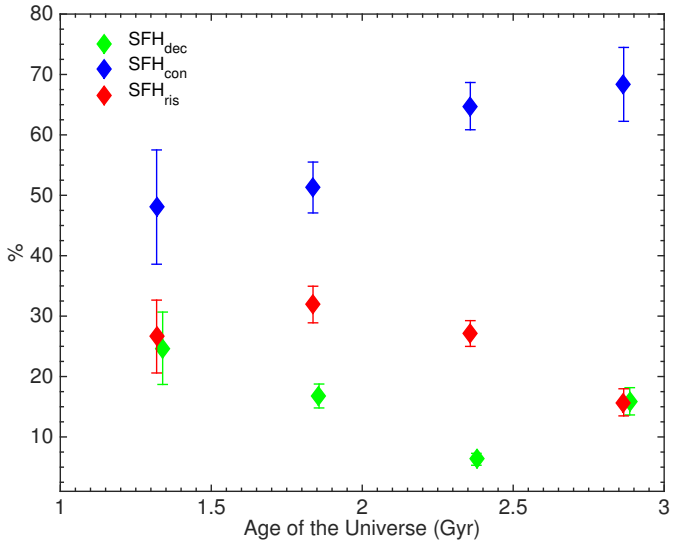

Fig. 10. Variation in the percentage of galaxies fit by different SFHs with the age of the Universe. The symbols are color coded according to the SFH. The green points have been slightly shifted to avoid overlap with the red ones.

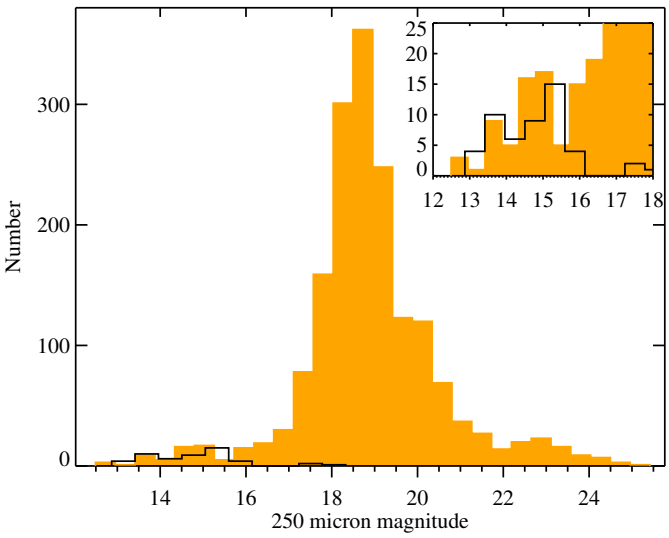

Fig. 11. Distribution of the 250 μm magnitudes in the COSMOS field. The yellow histogram refers to the magnitudes estimated by the SED fitting procedure, while the solid black line shows the distribution of the magnitudes observed by *Herschel*.

Data Centre as part of the Canada-France-Hawaii Telescope Legacy Survey, a collaborative project of NRC and CNRS.

References

Alongi, M., Bertelli, G., Bressan, A., et al. 1993, A&AS, 97, 851
Álvarez-Márquez, J., Burgarella, D., Heinis, S., et al. 2016, A&A, 587, A122
Arnouts, S., Cristiani, S., Moscardini, L., et al. 1999, MNRAS, 310, 540
Band, D. L., & Grindlay, J. E. 1985, ApJ, 298, 128
Bell, E. F., & de Jong, R. S. 2000, MNRAS, 312, 497
Bernhard, E., Béthermin, M., Sargent, M., et al. 2014, MNRAS, 442, 509
Bertelli, G., Bressan, A., Chiosi, C., Fagotto, F., & Nasi, E. 1994, A&AS, 106, 275
Bielby, R., Hill, M. D., Shanks, T., et al. 2013, MNRAS, 430, 425
Bressan, A., Fagotto, F., Bertelli, G., & Chiosi, C. 1993, A&AS, 100, 647
Bressan, A., Chiosi, C., & Fagotto, F. 1994, ApJS, 94, 63
Bruzual, A. G. 2007, in IAU Symp. 241, eds. A. Vazdekis, & R. Peletier, 125
Bruzual, G., & Charlot, S. 2003, MNRAS, 344, 1000
Buat, V., Noll, S., Burgarella, D., et al. 2012, A&A, 545, A141
Buzzoni, A. 2002, AJ, 123, 1188
Calzetti, D., Kinney, A. L., & Storchi-Bergmann, T. 1994, ApJ, 429, 582
Calzetti, D., Armus, L., Bohlin, R. C., et al. 2000, ApJ, 533, 682
Cardamone, C. N., van Dokkum, P. G., Urry, C. M., et al. 2010, ApJS, 189, 270

Cassarà, L. P. 2012, Ph.D. Thesis, University of Padova, Italy
Cassarà, L. P., Piovan, L., Weiss, A., Salaris, M., & Chiosi, C. 2013, MNRAS, 436, 2824
Cassarà, L. P., Piovan, L., & Chiosi, C. 2015, MNRAS, 450, 2231
Chiosi, C. 1980, A&A, 83, 206
Conroy, C. 2013, ARA&A, 51, 393
Conroy, C., Gunn, J. E., & White, M. 2009, ApJ, 699, 486
Conroy, C., Schiminovich, D., & Blanton, M. R. 2010, ApJ, 718, 184
da Cunha, E., Charlot, S., & Elbaz, D. 2008, MNRAS, 388, 1595
Daddi, E., Dickinson, M., Morrison, G., et al. 2007, ApJ, 670, 156
Davis, M., Faber, S. M., Newman, J., et al. 2003, in Discoveries and Research Prospects from 6- to 10-Meter-Class Telescopes II, ed. P. Guhathakurta, SPIE Conf. Ser., 4834, 161
de Barros, S., Schaerer, D., & Stark, D. P. 2014, A&A, 563, A81
Elbaz, D., Daddi, E., Le Borgne, D., et al. 2007, A&A, 468, 33
Fagotto, F., Bressan, A., Bertelli, G., & Chiosi, C. 1994a, A&AS, 104, 365
Fagotto, F., Bressan, A., Bertelli, G., & Chiosi, C. 1994b, A&AS, 105, 29
Fagotto, F., Bressan, A., Bertelli, G., & Chiosi, C. 1994c, A&AS, 105, 39
Faisst, A. L., Capak, P., Hsieh, B. C., et al. 2016, ApJ, 821, 122
Finkelstein, S. L., Papovich, C., Giavalisco, M., et al. 2010, ApJ, 719, 1250
Finlator, K., Davé, R., & Oppenheimer, B. D. 2007, MNRAS, 376, 1861
Finlator, K., Oppenheimer, B. D., & Davé, R. 2011, MNRAS, 410, 1703
Fioc, M., & Rocca-Volmerange, B. 1997, A&A, 326, 950
Franzetti, P., Scodeggio, M., Garilli, B., Fumana, M., & Paioro, L. 2008, in Astronomical Data Analysis Software and Systems XVII, eds. R. W. Argyle, P. S. Bunclark, & J. R. Lewis, ASP Conf. Ser., 394, 642
Fumagalli, M., Labbé, I., Patel, S. G., et al. 2014, ApJ, 796, 35
Girardi, L., Bressan, A., Chiosi, C., Bertelli, G., & Nasi, E. 1996, A&AS, 117, 113
Gonzalez-Perez, V., Lacey, C. G., Baugh, C. M., Frenk, C. S., & Wilkins, S. M. 2013, MNRAS, 429, 1609
Grevesse, N., & Noels, A. 1993, Phys. Scripta T, 47, 133
Guo, Y., Giavalisco, M., Cassata, P., et al. 2012, ApJ, 749, 149
Ilbert, O., Arnouts, S., McCracken, H. J., et al. 2006, A&A, 457, 841
Ilbert, O., Capak, P., Salvato, M., et al. 2009, ApJ, 690, 1236
Ilbert, O., Salvato, M., Le Floc'h, E., et al. 2010, ApJ, 709, 644
Ilbert, O., McCracken, H. J., Le Fèvre, O., et al. 2013, A&A, 556, A55
Kashikawa, N., Shimasaku, K., Matsuda, Y., et al. 2011, ApJ, 734, 119
Kennicutt, Jr., R. C. 1998, ApJ, 498, 541
Laigle, C., McCracken, H. J., Ilbert, O., et al. 2016, ApJS, 224, 24
Le Fèvre, O., Vettolani, G., Garilli, B., et al. 2005, A&A, 439, 845
Le Fèvre, O., Cassata, P., Cucciati, O., et al. 2013, A&A, 559, A14
Le Fèvre, O., Tasca, L. A. M., Cassata, P., et al. 2015, A&A, 576, A79
Lee, S.-K., Idzi, R., Ferguson, H. C., et al. 2009, ApJS, 184, 100
Lee, S.-K., Ferguson, H. C., Somerville, R. S., Wiklind, T., & Giavalisco, M. 2010, ApJ, 725, 1644
Lemaux, B. C., Le Floc'h, E., Le Fèvre, O., et al. 2014, A&A, 572, A90
Li, A., & Draine, B. T. 2001, ApJ, 554, 778
Madau, P. 1995, ApJ, 441, 18
Madau, P., & Dickinson, M. 2014, ARA&A, 52, 415
Mancuso, C., Lapi, A., Shi, J., et al. 2016, ApJ, 823, 128
Maraston, C. 2005, MNRAS, 362, 799
Maraston, C., Daddi, E., Renzini, A., et al. 2006, ApJ, 652, 85
Maraston, C., Pforr, J., Renzini, A., et al. 2010, MNRAS, 407, 830
Marigo, P., Girardi, L., Bressan, A., et al. 2008, A&A, 482, 883
Matteucci, F., & Pipino, A. 2002, ApJ, 569, L69
Mitchell, P. D., Lacey, C. G., Baugh, C. M., & Cole, S. 2013, MNRAS, 435, 87
Nagamine, K. 2000, BAAS, 32, 117.06
Noeske, K. G., Weiner, B. J., Faber, S. M., et al. 2007, ApJ, 660, L43
Noll, S., Burgarella, D., Giovannoli, E., et al. 2009, A&A, 507, 1793
Ouchi, M., Shimasaku, K., Akiyama, M., et al. 2008, ApJS, 176, 301
Panuzzo, P., Granato, G. L., Buat, V., et al. 2007, MNRAS, 375, 640
Papovich, C., Dickinson, M., & Ferguson, H. C. 2001, ApJ, 559, 620
Papovich, C., Finkelstein, S. L., Ferguson, H. C., Lotz, J. M., & Giavalisco, M. 2011, MNRAS, 412, 1123
Pforr, J., Maraston, C., & Tonini, C. 2012, MNRAS, 422, 3285
Piovan, L., Tantalo, R., & Chiosi, C. 2006a, MNRAS, 366, 923
Piovan, L., Tantalo, R., & Chiosi, C. 2006b, MNRAS, 370, 1454
Piovan, L., Chiosi, C., Merlin, E., et al. 2011, ArXiv e-prints [arXiv:1107.4541]
Pipino, A., & Matteucci, F. 2011, A&A, 530, A98
Pipino, A., Calura, F., & Matteucci, F. 2013, MNRAS, 432, 2541
Portinari, L., & Chiosi, C. 1999, A&A, 350, 827
Portinari, L., & Chiosi, C. 2000, A&A, 355, 929
Portinari, L., Chiosi, C., & Bressan, A. 1998, A&A, 334, 505
Portinari, L., Moretti, A., Chiosi, C., & Sommer-Larsen, J. 2004, ApJ, 604, 579
Reddy, N. A., Pettini, M., Steidel, C. C., et al. 2012, ApJ, 754, 25
Rodighiero, G., Daddi, E., Baronchelli, I., et al. 2011, ApJ, 739, L40
Rodighiero, G., Renzini, A., Daddi, E., et al. 2014, MNRAS, 443, 19
Salmon, B., Papovich, C., Finkelstein, S. L., et al. 2015, ApJ, 799, 183
Sawicki, M., & Yee, H. K. C. 1998, AJ, 115, 1329
Schaerer, D., & Pelló, R. 2005, MNRAS, 362, 1054
Schaerer, D., de Barros, S., & Sklias, P. 2013, A&A, 549, A4
Schmidt, M. 1959, ApJ, 129, 243
Scudder, J. M., Oliver, S., Hurley, P. D., et al. 2016, MNRAS, 460, 1119
Steidel, C. C., Adelberger, K. L., Shapley, A. E., et al. 2003, ApJ, 592, 728
Takagi, T., Vansevicius, V., & Arimoto, N. 2003, PASJ, 55, 385
Tantalo, R., Chiosi, C., Bressan, A., & Fagotto, F. 1996, A&A, 311, 361
Tasca, L. A. M., Le Fèvre, O., Hathi, N. P., et al. 2015, A&A, 581, A54
Thomas, D., Maraston, C., Bender, R., & Mendes de Oliveira, C. 2005, ApJ, 621, 673
Thomas, R., Le Fèvre, O., Scodeggio, M., et al. 2016, A&A, submitted [arXiv:1602.01841]
Tinsley, B. M. 1980, ApJ, 5, 287
Toft, S., Smolčić, V., Magnelli, B., et al. 2014, ApJ, 782, 68
Vanzella, E., Giavalisco, M., Dickinson, M., et al. 2009, ApJ, 695, 1163
Villaume, A., Conroy, C., & Johnson, B. D. 2015, ApJ, 806, 82
Weiss, A., & Ferguson, J. W. 2009, A&A, 508, 1343
Weiss, A., & Schlattl, H. 2008, Ap&SS, 316, 99
Wild, V., Charlot, S., Brinchmann, J., et al. 2011, MNRAS, 417, 1760
Wuyts, S., Förster Schreiber, N. M., van der Wel, A., et al. 2011, ApJ, 742, 96
Yabe, K., Ohta, K., Iwata, I., et al. 2009, ApJ, 693, 507
Zibetti, S., Gallazzi, A., Charlot, S., Pasquali, A., & Pierini, D. 2012, in IAU Symp. 284, eds. R. J. Tuffs, & C. C. Popescu, 63

[1] INAF–IASF Milano, via Bassini 15, 20133, Milano, Italy
e-mail: letizia.cassara@gmail.com
[2] INAF–Osservatorio Astronomico di Bologna, via Ranzani,1, 40127 Bologna, Italy
[3] Aix Marseille Université, CNRS, LAM (Laboratoire d'Astrophysique de Marseille) UMR 7326, 13388 Marseille, France
[4] INAF–Osservatorio Astronomico di Roma, via di Frascati 33, 00040 Monte Porzio Catone, Italy
[5] University of Bologna, Department of Physics and Astronomy (DIFA), V.le Berti Pichat, 6/2, 40127 Bologna, Italy
[6] INAF–IASF Bologna, via Gobetti 101, 40129 Bologna, Italy
[7] Institut d'Astrophysique de Paris, UMR7095 CNRS, Université Pierre et Marie Curie, 98 bis boulevard Arago, 75014 Paris, France
[8] Institut de Recherche en Astrophysique et Planétologie – IRAP, CNRS, Université de Toulouse, UPS-OMP, 14, avenue E. Belin, 31400 Toulouse, France
[9] Department of Astronomy, University of Geneva, ch. d'Ecogia 16, 1290 Versoix, Switzerland
[10] Geneva Observatory, University of Geneva, ch. des Maillettes 51, 1290 Versoix, Switzerland
[11] Centro de Estudios de Física del Cosmos de Aragón, 44001 Teruel, Spain
[12] Department of Astronomy, California Institute of Technology, 1200 E. California Blvd., MC 249–17, Pasadena, CA 91125, USA
[13] Astronomy Department, University of Massachusetts, Amherst, MA 01003, USA
[14] Max-Planck-Institut für Extraterrestrische Physik, Postfach 1312, 85741 Garching bei München, Germany
[15] Research Center for Space and Cosmic Evolution, Ehime University, Bunkyo-cho 2-5, 790-8577 Matsuyama, Japan
[16] SUPA, Institute for Astronomy, University of Edinburgh, Royal Observatory, Edinburgh, EH9 3HJ, UK
[17] Space Telescope Science Institute, 3700 San Martin Drive, Baltimore, MD 21218, USA
[18] Instituto de Fisica y Astronomia, Facultad de Ciencias, Universidad de Valparaiso, Av. Gran Bretana 1111, Casilla 5030, Valparaiso, Chile
[19] Institute for Astronomy, Astrophysics, Space Applications and Remote Sensing, National Observatory of Athens, Penteli, 15236 Athens, Greece

Appendix A: Models: single stellar populations

A detailed description of the features and novelties of the SSPs models can be found in Cassarà et al. (2013), here we briefly summarize their main characteristics:

- The Bertelli et al. (1994) library up to the end of the E-AGB and a new treatment of the AGB phase for the intermediate- and low-mass stars (Weiss & Ferguson 2009) were adopted.
- The stellar models of the Bertelli et al. (1994) library are those of Alongi et al. (1993), Bressan et al. (1993), Fagotto et al. (1994a,b,c), Girardi et al. (1996) and were calculated with the Padua stellar evolution code.
- The models of Weiss & Ferguson (2009) were calculated with the Garching stellar evolution code (Weiss & Schlattl 2008).
- All evolutionary phases, from the zero-age main sequence to the start of the TP-AGB stage or central C ignition were included.
- The age ranges from 0.005 to 20 Gyr (65 values of ages in total).
- The wavelength range extends from 0.1 to 1000 μm (rest frame).
- Five metallicity values (Z = 0.0004, 0.004, 0.008, 0.02 – the solar value – and 0.05) were employed.
- The primordial He-content is $Y = 0.23$ and the enrichment law is $\Delta Y/\Delta Z = 2.5$; given the metallicity Z and the helium content Y, the Grevesse & Noels (1993) abundance tables of heavy elements that compose the total metallicity were considered.

The local effect of absorption or emission due to the molecular clouds mimics the effect of the dust around the stellar population. It is calculated by applying the ray-tracing technique, which considers a dust component emitting in the IR and fully conserves the energy balance between the dust-absorbed stellar emission in the UV-optical range and its re-emission in the IR (Takagi et al. 2003; Piovan et al. 2006a).

A.1. Treatment of dust extinction and re-emission: the ray-tracing technique

The best way to include attenuation from interstellar dust in the modeling of stellar populations in galaxies is to solve the radiative transfer equation to build physical and self-consistent galactic SEDs (Panuzzo et al. 2007; Buat et al. 2012; Conroy 2013).

With the availability of mid- and far-IR data for large samples of galaxies, new codes that combine stellar and dust emission on the basis of the balance between the stellar luminosity absorbed by dust and the corresponding luminosity re-emitted in the IR are emerging (to mention only a few: da Cunha et al. 2008; Noll et al. 2009).

These codes make use of attenuation laws, with the exception of those that include a full radiation transfer treatment.

The most popular attenuation curve in use is the Calzetti law (Calzetti et al. 1994, 2000), which has been built for local starburst galaxies and is also used to include dust attenuation by fixing the shape of the attenuation curve and fitting for the normalization. It is worth underlining that the Calzetti law does not exhibit the bump at 2175 Å: on the contrary, in all radiative transfer dust models the expectation is that normal SFGs should show evidence of this dust feature provided that the underlining grain population is similar to that of MW or LMC, even if the question is still under debate because of the paucity of rest-frame UV spectra of SFGs (Conroy 2013).

Noll et al. (2009) presented stacked rest-frame UV spectra of $z \sim 2$ SFGs and found strong evidence of the 2175 Å feature with a strength slightly weaker than observed in the MW extinction curve, and Wild et al. (2011), in the UV, found evidence of a bump in the attenuation curve of spiral galaxies at 2175 Å (see also Conroy et al. 2010).

This feature could have a significant effect on the interpretation of high-redshift galaxies (Gonzalez-Perez et al. 2013; Mitchell et al. 2013).

To account for the effect of extinction and re-emission by dust, we adopted the ray-tracing radiative transfer code (see Takagi et al. 2003; Piovan et al. 2006a, for an exhaustive treatment of the topic). The radiative transfer code considers the cloud (MC hereafter) as a spherical object with dust, gas, and stars having the same spatial distribution across the whole region. The equation of radiative transfer (needed because the high density in the regions of star formation leads to a very high optical depth, also for IR photons) is solved along a set of rays traced throughout the inhomogeneous spherically symmetric source, and the effect of absorption and scattering of the light due to the dust of the molecular clouds is taken into account.

The spherical symmetry of the problem gives the possibility of calculating the specific intensity of the radiation field at a given distance from the center of the MC by averaging the intensities of all rays passing through that point (Band & Grindlay 1985).

When the SSP illuminating dust is specified, typical parameters of the MC are

- R: scale radius of the cloud: more or less compact MCs;
- b_c: the abundance of very small carbonaceous grains (VSGs, e.g., PAHs, and very small graphite grains) that particularly influence the MIR emission;
- *ion*: the ionization model of PAHs;
- τ_V: the optical depth of the cloud at a fixed wavelength (for example, in the V band).

The key parameter is the optical depth of the MCs. Its effect on the spectrum emitted by the cloud is that the higher the optical depth, the greater the amount of energy that is shifted toward longer wavelengths. The amount of IR re-emitted luminosity first quickly increases at increasing optical depth, then becomes less sensitive to τ_V and tends to flatten out for high τ_V (Piovan et al. 2006a).

The database of dusty SSPs was calculated considering

1. Z: five values of metallicity and 40 values of age for each metallicity;
2. R: scale radius of the cloud normalized to the SSP mass. R links the mass of the radiation sources to the dimension of the cloud, and its effect is to change the position of the FIR peak that is due to dust emission. An ideal MC scaled with a higher value of R will have a lower temperature profile of grains because of the larger dimensions.
3. τ_V: the optical depth of the cloud in the V band: 20 values of τ_V: 0.01, 0.03, 0.05, 0.08, 0.1, 0.3, 0.5, 0.8, 1, 1.3, 1.5, 1.8, 2, 2.3, 2.5, 2.8, 3, 3.3, 3.5, and 4 were adopted;
4. b_c: the abundances of VSGs: this parameter is related to the extinction curve (Piovan et al. 2006a) and was kept fixed to its highest value (except for the SMC extinction curve, where only one value is available);
5. *ion*: together with b_c, this parameter affects the PAHs emission. We used the ionization profile calculated in Li & Draine (2001) for the diffuse ISM of the MW;

6. *extinction curves*: we used three extinction curves (MW, LMC, and SMC). This parameter is related to the metallicity of the stellar populations whose radiation will be reprocessed from the MC.

These dusty SSPs are the seeds of theoretical models of galaxies. The last point to underline is that the adopted choices for τ_V, b_c, the ionization model of PAHs, and the extinction curves were applied to reduce the number of free parameters. As widely discussed in Piovan et al. (2006a), the ideal case would be to set up a library of SSPs that cover an ample range of optical depths by varying the mass and ratio of the molecular clouds. For our purpose, it is adequate to fix the parameter controlling the MIR and the FIR emission (Takagi et al. 2003; Piovan et al. 2006a) while varying the values of the optical depths, the key parameter of the radiative transfer problem, for which an ample range of values was allowed.

Appendix B: Composite stellar populations (CSPs models)

A model galaxy with a certain star formation history SFH, $SFR(t)$ and chemical enrichment history, $Z(t)$, can be modeled as the convolution of SSPs of different age, weighted by the SFR and chemical composition. We started from the database of dusty SSPs presented before and calculated a set of theoretical galaxies considering 28 SFHs with different ratios of infall time $\tau_{\rm infall}$ to star formation efficiency ν to model various morphological types (Buzzoni 2002; Piovan et al. 2006b). The main features and parameters involved in the galactic models are:

- *the galactic mass $M(t_{\rm Gal})$*: in the infall models, it represents the asymptotic value reached by the inflowing material at the final galaxy age. The age $t_{\rm Gal}$ is one of the inputs of the spectro-photometric code and it is fixed after the cosmological framework, and in particular the age of galaxy formation, is established. The galactic mass is expressed in $10^{12} \times M_\odot$;
- k: the exponent k of the Schmidt law (see Appendix B.1): for all models, $k = 1$;
- ν: the efficiency ν of the star formation rate is related to the galactic mass when simulating bulge galaxies to reproduce the observed trend of less massive galaxies that keep forming stars over a longer period with respect to more massive ones (Tantalo et al. 1996; Thomas et al. 2005), while $\nu = 0.50$ and 0.35, following Portinari et al. (1998) and Cassarà et al. (2015) in case of disk models;
- $\tau_{\rm infall}$: the infall timescale. $\tau_{\rm infall} = 0.3$ Gyr for bulge models and $\tau_{\rm infall} = 0.70$, 1, 3, 5 to account for a different time-extended star formation in disk galaxies (Portinari & Chiosi 1999, 2000).
- *slope and ζ of the IMF*: the slope is kept constant at the classical Salpeter value, whereas for ζ we adopted three values, $\zeta = 0.50$, 0.39, and 0.35. As first reported in Bressan et al. (1994) and subsequently discussed in Cassarà et al. (2015), the use of the Salpeter law for the IMF requires a proportionality constant. This constant was fixed by imposing that the fraction ζ of the IMF mass comprised between 1 $M_\odot$ (the lowest mass whose age is comparable to the age of the Universe) and the upper limit, that is, the mass interval that effectively contributes to nucleosynthesis. This parameter affects the metallicities of the galactic models.

The constraint of relating the efficiency of the star formation rate to the galactic mass for the bulge galaxies when the chemical evolution of the models is built comes from the following considerations. The chemical model in use is static, this means that the formation of the galaxy is simulated by the collapse of primordial gas in presence of the dark matter in a simple fashion. The model galaxy is conceived as a mass point (Chiosi 1980) for which no information about the spatial distribution of stars and gas is available. This classical chemical simulation adopts the star formation as an input. To reproduce the observed trend that the longest duration of star formation decreases with the galactic mass, we need to relate the efficiency of the star formation to $M(t_{\rm Gal})$. For a detailed discussion of this topic we refer to Tantalo et al. (1996), Piovan et al. (2006b), Cassarà (2012), Cassarà et al. (2015).

Table B.1. Parameters for galaxy models.

$M(t_{\rm Gal})$	ν	ζ	$\tau_{\rm infall}$
5.00	14.00	0.50	0.30
3.00	12.00	0.50	0.30
1.00	7.20	0.50	0.30
0.50	5.20	0.50	0.30
0.10	3.00	0.50	0.30
5.00	14.00	0.39	0.30
3.00	12.00	0.39	0.30
1.00	7.20	0.39	0.30
0.50	5.20	0.39	0.30
0.10	3.00	0.39	0.30
1.00	7.20	0.50	0.70
3.00	12.00	0.50	0.70
0.50	5.20	0.50	0.70
1.00	0.50	0.35	1.00
1.00	0.50	0.35	3.00
1.00	0.50	0.35	5.00
1.00	0.50	0.50	1.00
1.00	0.50	0.50	3.00
1.00	0.50	0.50	5.00
1.00	0.35	0.50	1.00
1.00	0.35	0.50	3.00
1.00	0.35	0.50	5.00
1.00	0.50	0.50	0.50
1.00	0.50	0.35	0.50
1.00	0.35	0.50	0.50
1.00	1.00	0.50	0.50
1.00	1.50	0.50	0.50
1.00	2.00	0.50	0.50

Typical resulting evolutionary galaxy SEDs are shown in Fig. B.1: the upper panel shows the evolution with the age of the stellar populations, while the lower panel depicts SEDs derived by varying the optical depth of the MCs.

The real advantage of full and physically consistent SEDs that extend from the far-UV to the FIR is that they reveal important components of a galaxy that are not noticeable in the UV where young, massive stars are the dominant flux contributor.

Our library of model galaxies consists of ∼30 000 models: 28 galactic models ×20 optical depths τ_V × ∼ 55 values of age for each evolutionary model.

It is worth underlining that these types of evolutionary galaxy models with different morphological types are able to reproduce CMDs of local galaxies and the color-redshift evolution (Bressan et al. 1994; Piovan et al. 2006b; Cassarà et al. 2015).

B.1. Star formation rate and histories

The star formation and chemical enrichment histories of this type of theoretical galaxy models are fully described in several papers (Chiosi 1980; Tantalo et al. 1996; Portinari et al. 1998; Piovan et al. 2006b) and are not repeated here. We recall the most important points. The star formation rate, that is, the number of stars of mass M born in the time interval dt and mass interval dM, is given by $\mathrm{d}N/\mathrm{d}t = \Psi(t)SFR(M)\mathrm{d}M$.

The star formation rate $SFR(t)$ is the (Schmidt 1959) law adapted to the models, $SFR(t) = \nu M_{\rm g}(t)^k$, where $M_{\rm g}$ is the mass of the gas at the time t. The parameter ν and k are extremely important: k yields the dependence of the SFR on the gas content, while ν measures the efficiency of the star formation process. Because of the competition between gas infall, gas consumption by star formation, and gas ejection by dying stars, the SFR starts very low in this type of models, grows to a maximum and then declines.

The timescale roughly corresponds to the age at which the star formation activity reaches the peak value.

The last point worth emphasizing is that the galaxy models rely on a robust model of chemical evolution that, assuming a suitable prescription for gas infall, IMF, SFR, and stellar ejecta, provides the total amounts of gas and stars present at any age together with their chemical histories, to be used as entries for the population synthesis code (Chiosi 1980; Tantalo et al. 1996; Portinari et al. 1998; Portinari & Chiosi 2000; Piovan et al. 2006a,b; Cassarà et al. 2015).

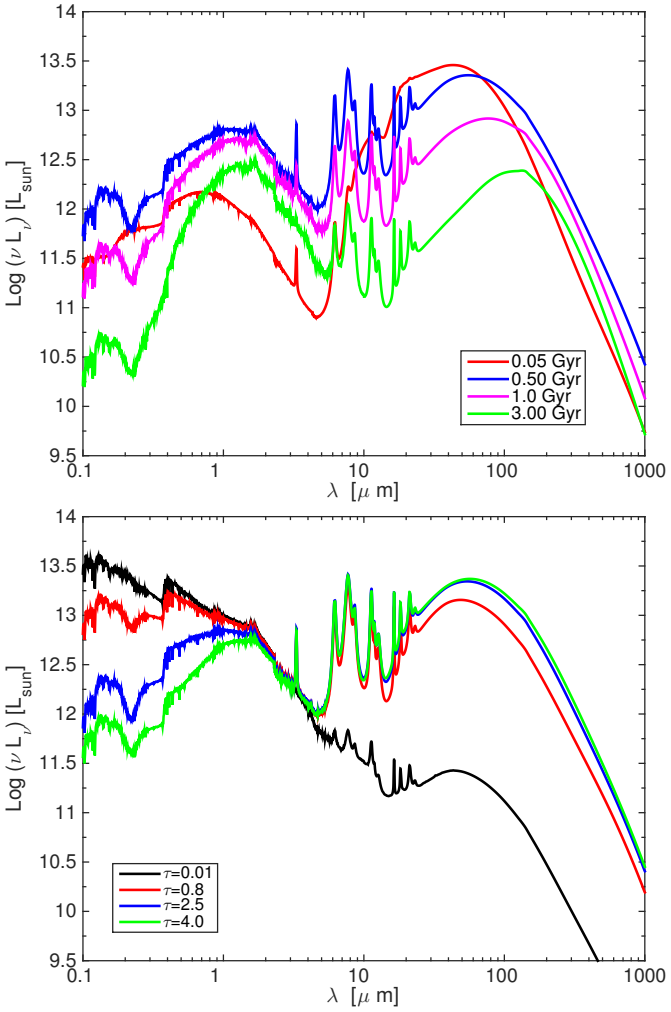

Fig. B.1. SEDs of theoretical galaxies at different ages and for τ_V = 2.5 (*upper panel*) and with different optical depths of the MC τ_V and t = 0.75 Gyr (*lower panel*).